THE STUDY OF ION TRANSPORT MECHANISMS IN NANOFILTRATION MEMBRANES WITH CONSTANT SURFACE POTENTIAL / CHARGE DENSITY

Ilya I. Ryzhkov [a1] and Andrey V. Minakov [b]

[a] *Institute of Computational Modelling SB RAS, Akademgorodok, 660036 Krasnoyarsk, Russia, e-mail: rii@icm.krasn.ru*

[b] *Institute of Engineering Physics and Radio Electronics, Siberian Federal University, Svobodny 79, 660041 Krasnoyarsk, Russia, e-mail: tov–andrey@yandex.ru*

Abstract. The pressure–driven ion transport through nanofiltration membrane pores with constant surface potential or charge density is investigated theoretically. Two approaches are employed in the study. The first one is based on one–dimensional Nernst–Planck equation coupled with electroneutrality, zero current, and Donnan equilibrium conditions. This model is extended to account for interfacial effects by using a smooth approximation of step function for the volume charge density. A simplified model for the case of constant surface potential is also proposed. The second approach is based on two–dimensional Nernst–Planck, Poisson, and Navier–Stokes equations, which are solved in a high aspect ratio nanopore connecting two reservoirs with much larger diameter. The modification of equations on the basis of Slotboom transformation is employed to speed up the convergence rate. The distributions of potential, pressure, ion concentrations and fluxes due to convection, diffusion, and migration in the nanopore and reservoirs are discussed and analyzed. It is found that for constant surface charge density, the convective flux of counter–ions in the nanopore is almost completely balanced by the opposite migration flux, while for constant surface potential, the convective flux is balanced by the opposite diffusion and migration fluxes. The co–ions in the nanopore are mainly transported by diffusion. A particular attention is focused on describing the interfacial effects at the nanopore entrance/exit. Detailed comparison between one– and two–dimensional models is performed in terms of rejection, pressure drop, and membrane potential dependence on the surface potential/charge density, volume flux, electrolyte concentration, and pore radius. A good agreement between these models is found when the Debye length is smaller than the pore radius and the surface potential or charge density are sufficiently low.

Keywords: nanofiltration, charged membranes, electrolyte transport, interfacial effects, numerical modelling

1 Introduction

Nanofiltration (NF) is a pressure–driven membrane process, which is used to remove ionic species and organic solutes from aqueous solutions [1]. Nanofiltration membranes are characterized by effective pore diameter ranging from one to a few nanometers, and the molecular weight cut–off between a few hundred to a few thousand Dalton. The range of operating pressure starts from a few bars up to 10–20 bars. These characteristics lie between those of reverse osmosis (RO) and ultrafiltration (UF) membranes [2]. NF membranes combine the advantages of a high water flux at relatively low operating pressure and high salt and organic matter rejection rate [3]. Nanofiltration has received much attention in the last decades due to its applications in textile, paper, and food industries including water desalination [1–4].

[1] Corresponding author

The separation mechanisms of NF membranes include not only steric, but also electric effects. Most of such membranes acquire an electric charge when brought in contact with a polar medium due to dissociation of functional groups or adsorption of charged species from the solution onto the pore walls. In nanometer–sized pores, the electric double layers from the opposite walls overlap, which leads to the favoured transport of counter–ions and exclusion of co–ions. If the pore walls are made of conductive material, the wall charge can be altered by applying a prescribed potential to the membrane. In this way, the membrane selectivity characteristics can be externally varied and controlled [5,6]. A comprehensive review of charged membranes applications can be found in [7].

The development of adequate mathematical models for nanofiltration is extremely important for better understanding of complex transport mechanisms and prediction of separation characteristics [8]. A charged membrane is usually modelled as an array of identical parallel charged pores. It is now well established that the pressure–driven transport of ions in charged membrane pores can be described by the system of Nernst–Planck, Poisson, and Navier–Stokes equations [9]. However, the direct application of this model requires much computational resources even in two–dimensional statement. Due to that, a number of simplified approaches has been developed. In the homogeneous approximation [10], the uniform distribution of fixed charged in membrane pores is assumed, and the radial variation of electric potential and ion concentrations in the pore is neglected. It is a valid assumption when the Debye screening length is much larger than the pore radius, and the fixed charge density is sufficiently low. In this case, the model reduces to one–dimensional Nernst–Planck equation extended by convective transport term, the electroneutrality and zero current conditions, and Donnan equilibrium at the pore entrance and exit. This is known as Teorell–Meyer–Sievers (TMS) model. The latter was successfully applied for interpreting the experimental data on reverse osmosis in charged membranes in [11]. The Donnan–steric partitioning pore model (DSPM) [12] takes into account the finite ion size by introducing diffusive and convective hindrance factors. The fitting of experimental rejection data to this model allowed obtaining such membrane characteristics as pore radius, volume charge density, and effective membrane thickness [13–15]. The effect of concentration polarization on salt rejection was investigated in [16] by coupling the DSPM model with convection–diffusion equations in the boundary layer adjacent to the membrane. The contribution of convection, diffusion, and migration to electrolyte transport through nanofiltration membranes was studied in [17]. It was found that convection is the dominant transport mechanism at low membrane charge density and/or high permeate volume flux, while the transport is mainly governed by diffusion when the membrane is strongly charged. Migration becomes dominant when the co–ion diffusion coefficient exceeds that of counter–ion. The effect of inhomogeneous charge distribution on the pressure–driven ionic transport was considered in [18]. It was suggested that the rejection capability of nanopores can be optimized by the appropriate fixed charge distribution. For the case of bipolar charge distribution [19], similar rejection was found in asymmetric electrolytes with divalent co–ions or counter–ions. In contrast, homogeneously charged nanopores strongly reject the former type of electrolyte and are much more permeable to the latter one.

The radial variation of potential and ion concentrations in the pore as well as the impact of electroosmotic flow on ion transfer are taken into account in the space–charge (SC) model, which was originally developed in [20]. Detailed comparison between results obtained from SC and TMS models [21] showed a good agreement for pores with small radius (less than 2 nm) and low surface charge density. Otherwise, a strong overestimation of rejection by the TMS model in comparison with the SC model was found. Similar conclusion was made with respect to membrane potentials of monovalent and multivalent electrolytes calculated from the above two models in [22]. A simplification of SC model, which assumes a parabolic velocity profile (Poiseuille flow) in the pore, was suggested in [23]. Comparison between theory and experiment

on salt rejection in compacted clay showed a very good agreement.

The effect of membrane/solution interface on the distribution of potential and ion concentrations in the absence of pressure–driven flow was investigated in [24] by solving two–dimensional Nernst–Planck and Poisson equations in two reservoirs connected by a charged nanopore. The cases of equal and unequal electrolyte concentrations in the reservoirs were considered. In the latter case, it was found that unequal migration and diffusion currents resulted in non–zero total current flow in the system. A simplified analytical approach to describing potential distribution in the interfacial region was suggested in [25]. It was concluded that Donnan equilibrium conditions with discontinuous potential and ion concentrations at the interface are valid only if the membrane thickness is much greater than the Debye length. The impact of pressure–driven flow on the ion transfer in the nanopore connecting two reservoirs with equal electrolyte concentrations was investigated numerically in [26]. In addition to counter–ion enrichment and co–ion depletion in the nanopore, the increase/decrease of electrolyte concentration near the pore entrance/exit was found. The latter effect became stronger with increasing the applied pressure drop. The impact of electric force on pressure–driven flow (the electroviscous effect) in reservoir–connected flat and circular nanochannels was studied numerically in [27, 28]. A simple analytical model was suggested for prediction of the pressure drop and correlated with the numerical results. It should be noted that in the above–mentioned works, the nanopore diameter was of order 10–100 nm, while the length to the diameter ratio was of order 10. The considered electrolyte concentrations were 1 mol/m^3 and lower except the work [24] (the pressure–driven flow was not considered there). However, typical nanofiltration membranes have the pore diameter of a few nanometers and the aspect ratio of order 100–1000, while the electrolyte concentration can be as high as 1000 mol/m^3 [1–5].

The main aim of this work is to investigate theoretically the pressure–driven ion transport through nanofiltration membrane pores of realistic geometry in a wide range of electrolyte concentrations. The cases of constant surface charge density and constant surface potential are considered. Note that the former case has not been studied in details in the literature. Two approaches are employed in the study. The first one is based on one–dimensional Nernst–Planck equation coupled with electroneutrality, zero current, and Donnan equilibrium conditions. This model is extended to account for interfacial effects by using a smooth approximation of step function for the volume charge density. A simplified model for the case of constant surface potential is also proposed. The second approach is based on two–dimensional Nernst–Planck, Poisson, and Navier–Stokes equations, which are solved in a high aspect ratio nanopore, which connects two reservoirs with much larger diameter. The modification of equations on the basis of Slotboom transformation is employed to speed up the convergence rate. Detailed comparison between the two approaches is performed in terms of rejection, pressure drop, and membrane potential dependence on the applied potential/charge density, volume flux, electrolyte concentration, and pore radius. A particular attention is focused on describing the interfacial effects at the nanopore entrance/exit.

The paper is organized as follows. The mathematical models are presented in Section 2, while the numerical implementation is described in Section 3. The obtained results are analyzed and discussed in Section 4. The main findings are summarized in Conclusion.

2 Models formulation

2.1 One–dimensional model with specified surface charge density

Consider a cylindrical nanopore of length L_p and radius R_p, which connects two reservoirs of length L_r and radius R_r (Fig. 1). The surface charge density $\sigma_s(z)$ is specified at the

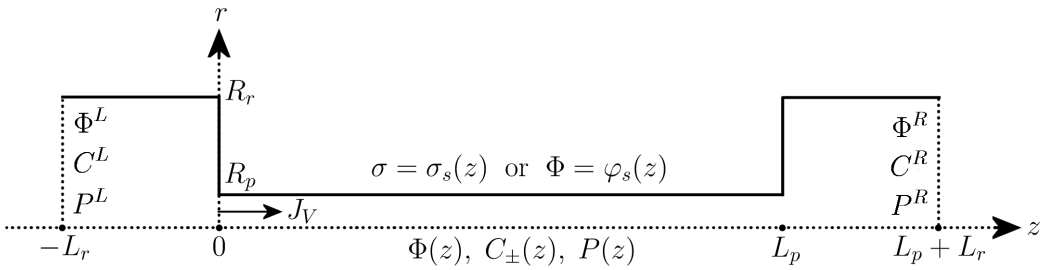

Figure 1: The geometry of the nanopore and reservoirs with notation for one–dimensional model.

nanopore wall, while the walls of reservoirs are not charged. In this paper, we consider the case of monovalent symmetric electrolyte, so all models will be formulated for this case for simplicity. The concentrations of positive and negative ions are denoted by C_+ and C_-, respectively. The ionic solution is pumped through the pore with the volume flux J_V, which is equivalent to the solution velocity. In the homogeneous approach, the electric potential Φ, ion concentrations $C_\pm$, and pressure P are functions of longitudinal coordinate z only. The molar fluxes of ions are described by the extended Nernst–Planck equation:

$$J_\pm = C_\pm J_V - D_\pm \frac{dC_\pm}{dz} \mp \frac{D_\pm F}{RT} C_\pm \frac{d\Phi}{dz}, \tag{1}$$

where $D_\pm$ are the ion diffusion coefficients, F is the Faraday constant, R is the ideal gas constant, and T is the temperature. Note that we do not take into account the hindrance factors for convection and diffusion [13–15] since our aim is to compare the results obtained from one– and two–dimensional models. The latter model is described in Section 2.3 and does not take into account the hindrance effects in the present formulation.

The conditions of no electric current and electroneutrality inside the nanopore and reservoirs are given by

$$J_+ - J_- = 0, \tag{2}$$

$$C_+ - C_- + X = 0, \qquad C_+^L - C_-^L = 0, \qquad C_+^R - C_-^R = 0. \tag{3}$$

Here $C_+^L = C_-^L = C^L$ and $C_+^R = C_-^R = C^R$ are the ion concentrations in the left and right reservoirs, respectively, while X is the effective volume charge density, which is related to the surface charge density σ_s by the formula

$$X = \frac{2\sigma_s}{FR_p}. \tag{4}$$

It is assumed that far from the pore exit in the right reservoir, the transport of ions occurs by convection only (there are no concentration and potential gradients). Together with equation (2) it leads to

$$J_\pm = C^R J_V. \tag{5}$$

Note that C^R is not known in advance and should be determined from the solution of the problem.

The Donnan equilibrium conditions at the nanopore entrance and exit are written as

$$C_\pm(0) = C^L \exp\left(\mp \frac{F}{RT}\Delta\Phi^L\right), \qquad C_\pm(L_p) = C^R \exp\left(\pm \frac{F}{RT}\Delta\Phi^R\right), \tag{6}$$

where $\Delta\Phi^L = \Phi(0) - \Phi^L$, $\Delta\Phi^R = \Phi^R - \Phi(L_p)$ are the potential jumps, while $\Phi(0)$, $C_\pm(0)$ and $\Phi(L_r)$, $C_\pm(L_r)$ are the potential and ion concentrations inside the nanopore near the entrance and exit, respectively. It follows from (3) and (6) that

$$C_\pm(0) = \frac{\mp X(0) + \sqrt{X^2(0) + 4(C^L)^2}}{2}, \qquad \Delta\Phi^L = \mp\frac{RT}{F}\ln\frac{C_\pm(0)}{C^L}, \tag{7}$$

$$C^R = \sqrt{C_+(L_p)\,C_-(L_p)}, \qquad \Delta\Phi^R = \pm\frac{RT}{F}\ln\frac{C_\pm(L_p)}{C^R}. \tag{8}$$

With the help of (5), equation (1) can be rewritten as

$$\frac{dC_\pm}{dz} = \frac{J_V\,(C_\pm - C^R)}{D_\pm} \mp \frac{F}{RT}\,C_\pm\frac{d\Phi}{dz}. \tag{9}$$

By differentiating the first equation in (3) and substituting the expression for $dC_\pm/dz$ from (9) into the result, we find

$$\frac{d\Phi}{dz} = \left(\frac{J_V\,(C_+ - C^R)}{D_+} - \frac{J_V\,(C_- - C^R)}{D_-} + \frac{dX}{dz}\right)\left(\frac{F}{RT}\,\big(C_+ + C_-\big)\right)^{-1}. \tag{10}$$

The equation for pressure can be obtained by taking z–momentum equation in the Navier–Stokes system and averaging it over the nanopore cross–section [18]:

$$\frac{dP}{dz} = -\frac{8\mu}{R_p^2}J_V - F(C_+ - C_-)\frac{d\Phi}{dz}, \tag{11}$$

where μ is the dynamic viscosity of ionic solution. In the derivation of (11), it is assumed that the velocity in z direction has a parabolic profile

$$V = 2J_V\Big(1 - (r/R_p)^2\Big).$$

The osmotic pressure jumps at the pore entrance/exit are given by

$$\Delta P^L = P(0) - P^L = RT\big(C_+(0) + C_-(0) - 2C^L\big), \tag{12}$$

$$\Delta P^R = P^R - P(L_p) = RT\big(2C^R - C_+(L_p) - C_-(L_p)\big). \tag{13}$$

The total pressure difference $\Delta P = P^L - P^R$ can be found by integrating equation (11) from $z = L_p$ to $z = 0$ with the help of (3) and taking into account the osmotic pressure jumps:

$$\Delta P = -\Delta P^L + \frac{8\mu L_p}{R_p^2}\,J_V + F\int\limits_{L_p}^{0} X\frac{d\Phi}{dz}dz - \Delta P^R. \tag{14}$$

The distributions of potential, ion concentrations, and pressure in the nanopore can be obtained by the following procedure. Given the values Φ^L, C^L, P^L, the values at the pore entrance $\Phi(0)$, $C_\pm(0)$, $P(0)$ are calculated from (7) and (12). Then an initial guess for C^R is set and equations (9)–(11) are integrated numerically from $z = 0$ to $z = L_p$. After that, the values of Φ^R, C^R, P^R are found from (8) and (13). The problem is solved iteratively until the initial guess for C^R at the current iteration coincides with the calculated value within the required accuracy.

It should be noted that the above–described approach does not allow detailed treatment of potential, ion concentrations, and pressure distribution as well as ion fluxes due to convection, diffusion, and migration in the interfacial regions. To overcome this limitation for nanopores

with constant surface charge density, we propose a simplified approach by considering the distribution of surface charge density $\sigma(z)$ with a smooth transition between zero value in the reservoirs and the constant value σ_s in the nanopore:

$$\sigma = \sigma_s\big(H(z) - H(z - L_p)\big), \qquad H(z) = \frac{1}{1 + e^{-2kz}}. \tag{15}$$

Here $H(z)$ is a smooth approximation of Heaviside step function and k is a constant. In this case, equations (9)–(11) can be integrated from $z = -L_r$ to $z = L_p + L_r$ with initial conditions $\Phi = \Phi^L$, $C_\pm = C^L$, $P = P^L$ at $z = -L_r$. For convenience, we take $\Phi^L = 0$. In equation (11), the nanopore radius R_p is replaced by the reservoir radius R_r and the volume flux J_V is replaced by $(R_p/R_r)^2\, J_V$ for $-L_r \leqslant z < 0$ and $L_p < z \leqslant L_p + L_r$. The pressure P^L is chosen to satisfy the condition $P^R = 0$. The explicit consideration of Donnan equilibrium conditions (7), (8) and osmotic pressure jumps (12), (13) is not required since all variables vary continuously in the interfacial regions. The results obtained by the proposed approach will be compared with the solution of two–dimensional model (Section 2.3), which takes into account the detailed geometry of nanopore and reservoirs.

The rejection (the fraction of ions, which is retained by the membrane) is calculated as

$$\mathrm{R} = 1 - \frac{C^R}{C^L}. \tag{16}$$

2.2 One–dimensional model with specified surface potential

In this section, we propose a simple modification of one–dimensional model for the case of specified potential $\varphi_s(z)$ on the nanopore wall. Since the potential in the right reservoir is not known in advance and should be determined from the solution of the problem, it is not possible to specify the distribution of potential in the nanopore and reservoirs in the form similar to (15). In the frame of homogeneous approach, we assume that the potential in the nanopore is the function of z only, so $\Phi(z) = \Phi^L + \varphi(z)$, where $\varphi(z) = \varphi_s(z)$. It follows that $\Delta\Phi^L = \Phi(0) - \Phi^L = \varphi(0)$. For convenience, we take $\Phi^L = 0$. Equation (9) in the nanopore can be solved analytically with the initial conditions given by (7):

$$C_\pm = \left[C_\pm(0)\exp\left(\pm\frac{F\varphi(0)}{RT}\right) - \frac{J_V C^R}{D_\pm}\int\limits_0^z \exp\left(-\frac{J_V}{D_\pm}z' \pm \frac{F\varphi(z')}{RT}\right)dz'\right]\exp\left(\frac{J_V}{D_\pm}z \mp \frac{F\varphi(z)}{RT}\right).$$

For $\varphi = \mathrm{const}$, this solution reduces to

$$C_\pm = C^R + \big(C_\pm(0) - C^R\big)\exp\left(\frac{J_V}{D_\pm}z\right).$$

The concentration C^R is determined from the first relation in (8), which reduces to the quadratic equation. It can be shown that for $\varphi = \mathrm{const}$ it has two real roots (positive and negative), so the physically meaningful positive solution for C^R always exists. The potential in the right reservoir is $\Phi^R = \varphi(L_p) + \Delta\Phi^R$, where $\Delta\Phi^R$ is given by the second relation in (8). The resulting volume charge density is determined from the first equation in (3). The integration of (11) gives the pressure distribution in the nanopore, while the total pressure drop is calculated from (14). The pressure inside the nanopore becomes linear $P = P(0) + 8\mu/R_p^2\, z$ when $\varphi = \mathrm{const}$.

2.3 Two–dimensional model

Let us now proceed to the two–dimensional model of pressure–driven flow and ion transport in a charged cylindrical nanopore of length L_p and radius R_p, which connects two reservoirs

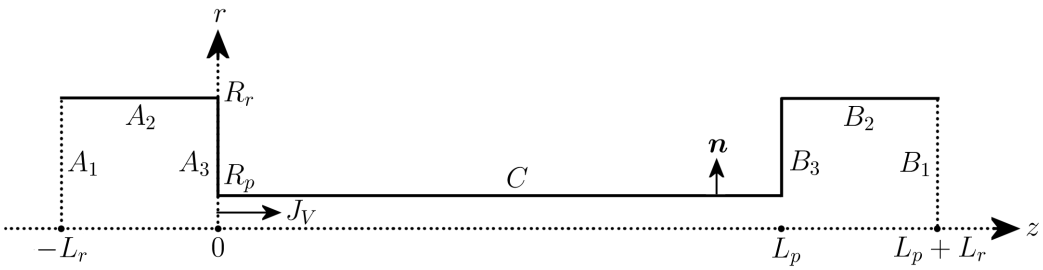

Figure 2: The geometry of the nanopore and reservoirs.

Table 1: The boundary conditions.

Boundary segment	Navier–Stokes equations	Poisson equation	Nernst–Planck equations	Nernst–Planck eqns. (Slotboom variables)
A_1	$U = 0,\ V = J'_V$	$\Phi = 0$	$C_\pm = 1$	$\widetilde{C}_\pm = 1$
B_1	$P = 0$	$\nabla\Phi \cdot \boldsymbol{n} = 0$	$(-\nabla C_\pm \mp C_\pm \nabla\Phi) \cdot \boldsymbol{n} = 0$	$\nabla\widetilde{C}_\pm \cdot \boldsymbol{n} = 0$
$A_{2,3}$, $B_{2,3}$	$U = V = 0$	$\nabla\Phi \cdot \boldsymbol{n} = 0$	$(-\nabla C_\pm \mp C_\pm \nabla\Phi) \cdot \boldsymbol{n} = 0$	$\nabla\widetilde{C}_\pm \cdot \boldsymbol{n} = 0$
C	$U = V = 0$	$\nabla\Phi \cdot \boldsymbol{n} = \sigma'_s$ or $\Phi = \varphi'_s$	$(-\nabla C_\pm \mp C_\pm \nabla\Phi) \cdot \boldsymbol{n} = 0$	$\nabla\widetilde{C}_\pm \cdot \boldsymbol{n} = 0$

of length L_r and radius R_r. The axisymmetric geometry of the system is shown in Fig. 2.

The flow and ion transport are described by the Navier–Stokes, Nernst–Plank, and Poisson equations. We introduce dimensionless variables by taking the characteristic scales of length L (to be specified later), velocity J_V, pressure ρJ_V^2, concentration C^L, and potential RT/F. The dimensionless governing equations are written in the form

$$(\boldsymbol{U} \cdot \nabla)\boldsymbol{U} = -\nabla P + \frac{1}{\mathrm{Re}}\nabla^2\boldsymbol{U} - \Lambda(C_+ - C_-)\nabla\Phi, \tag{17}$$

$$\nabla \cdot \boldsymbol{U} = 0, \tag{18}$$

$$\mathrm{Pe}\,\boldsymbol{U} \cdot \nabla C_+ = -\nabla \cdot (-\nabla C_+ - C_+\nabla\Phi), \tag{19}$$

$$\mathrm{Pe}\,\boldsymbol{U} \cdot \nabla C_- = -\nabla \cdot D(-\nabla C_- + C_-\nabla\Phi), \tag{20}$$

$$\nabla^2\Phi = -\frac{1}{2\lambda^2}(C_+ - C_-), \tag{21}$$

where $\boldsymbol{U}$ is the velocity vector. For axisymmetric problem, it is written as $\boldsymbol{U} = (U, V)$, where U and V are the radial and axial velocity components, respectively. The equations are solved in cylindrical coordinates. The dimensionless parameters of the problem are listed below:

$$\mathrm{Re} = \frac{\rho J_V L}{\mu}, \qquad \mathrm{Pe} = \frac{J_V L}{D_+}, \qquad \Lambda = \frac{RTC^L}{\rho J_V^2}, \qquad D = \frac{D_-}{D_+}, \tag{22}$$

$$\lambda = \frac{1}{L}\sqrt{\frac{\varepsilon\varepsilon_0 RT}{2C^L F^2}}, \qquad \varphi'_s = \frac{F\varphi_s}{RT}, \qquad \sigma'_s = \frac{FL\sigma_s}{\varepsilon\varepsilon_0 RT}, \qquad J'_V = \frac{R_p^2}{R_r^2}.$$

Here Re is the Reynolds number, Pe is Peclet number, Λ is the parameter, which characterizes the electric (Coulomb) force, D is the ratio of diffusion coefficients, λ is the dimensionless

Debye length, φ_s' and σ_s' are the dimensionless surface potential and surface charge density, respectively, and J_V' is the dimensionless velocity at the inlet. It is chosen from the condition of equal flow rates in the reservoirs and nanopore. In formulas (22), ρ is the density of ionic solution, ε is its relative permittivity, and ε_0 is the vacuum permittivity.

The boundary conditions are summarized in Table 1. An outward unit normal to the boundary is denoted by $\boldsymbol{n}$. At the inlet A_1, the constant dimensionless axial velocity J_V', zero potential, and constant dimensionless concentration are specified. At the outlet B_1, we impose zero pressure, the absence of potential gradient, and zero fluxes of ions due to diffusion and migration (the transport of ions occurs by convection only). The same conditions are specified on the reservoir walls A_2, A_3, B_2, B_3 except zero pressure requirement, which is replaced by the no–slip condition. The latter is also specified on the nanopore wall C together with zero diffusion and migration fluxes. In addition, we impose constant charge density or constant potential on the nanopore wall.

When the ions have equal diffusion coefficients ($D = 1$), the considered problem is invariant under the transformation

$$\Phi \to -\Phi, \qquad C_\pm \to C_\mp, \qquad \sigma_s' \to -\sigma_s' \qquad (\varphi_s' \to -\varphi_s'). \tag{23}$$

If the solution for a fixed sign of surface potential or charge density is known, the change of variables (23) provides the solution for the opposite sign of these parameters.

An alternative formulation of governing equations can be proposed by introducing the Slotboom variables [29–31] according to

$$C_\pm = e^{\mp\Phi}\widetilde{C}_\pm.$$

Using these variables, equations (17)—(21) are rewritten as

$$(\boldsymbol{U}\cdot\nabla)\boldsymbol{U} = -\nabla P + \frac{1}{\mathrm{Re}}\nabla^2\boldsymbol{U} - \Lambda\big(e^{-\Phi}\widetilde{C}_+ - e^{\Phi}\widetilde{C}_-\big)\nabla\Phi, \tag{24}$$

$$\nabla\cdot\boldsymbol{U} = 0, \tag{25}$$

$$\nabla\cdot\left(e^{-\Phi}\left(\mathrm{Pe}\,\boldsymbol{U}\widetilde{C}_+ - \nabla\widetilde{C}_+\right)\right) = 0, \tag{26}$$

$$\nabla\cdot\left(e^{\Phi}\left(\mathrm{Pe}\,\boldsymbol{U}\widetilde{C}_- - D\nabla\widetilde{C}_-\right)\right) = 0, \tag{27}$$

$$\nabla^2\Phi = -\frac{1}{2\lambda^2}\big(e^{-\Phi}\widetilde{C}_+ - e^{\Phi}\widetilde{C}_-\big). \tag{28}$$

After the transformation, the boundary conditions for Navier–Stokes and Poisson equations remain the same, while the conditions for the Nernst–Planck equations are transformed into a simpler form, which is given in the last column of Table 1. The advantages of using the Slotboom variables will be discussed further in Section 3.

It should be noted that the flow in nanopores typically corresponds to low Reynolds numbers, so the convective term in (17) and (24) can be neglected. However, we have retained it for completeness.

2.4 Physical parameters

In this paper, the calculations are performed for potassium chloride aqueous solution, which fully dissociate into K^+ and Cl^- ions. The parameters used are as follows: $T = 298.15$ K, $R = 8.314$ J/(mol K), $F = 96485$ C/mol, $\varepsilon = 78.49$, $\varepsilon_0 = 8.854\cdot10^{-12}$ F/m, $\rho = 997$ kg/m^3, $\mu = 0.888\cdot10^{-3}$ Pa·s, $D_+ = 1.957\cdot10^{-9}$ m^2/s, $D_- = 2.032\cdot10^{-9}$ m^2/s, $L = 10^{-9}$ m. The size of reservoirs is fixed to $R_r = 25$ nm, $L_r = 100$ nm, while the nanopore dimensions

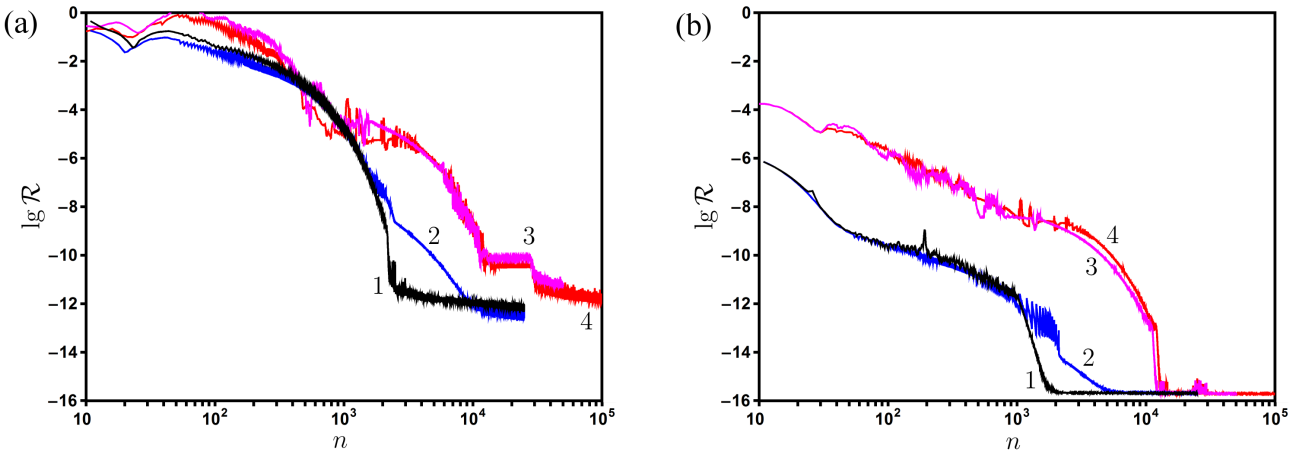

Figure 3: The dependence of residuals for continuity equation (a) and negative ion transport equation (b) on the number of iterations n. 1 – Coupled method, Slotboom variables; 2 – SIMPLEC method, Slotboom variables; 3 – Coupled method, Primitive variables; 4 – SIMPLEC method, Primitive variables.

can take the following values: $R_p = 1, 2, 5, 10$ nm, $L_p = 1000, 2000$ nm. In some cases (low values of inlet concentration and high values of surface potential/charge density), the length of right reservoir is extended to 300 nm to satisfy the condition $C_+ = C_-$ at the outlet. The value of constant k in (15) is chosen as 0.5 provided that the values of z are given in nanometers. It results in a smooth transition between $\sigma = 0$ and $\sigma = \sigma_s$ within 10 nm range of z at the nanopore entrance/exit. The variations of physical parameters C^L, J_V, φ_s, σ_s as well as dimensionless variables (22) are described in Section 4.

3 Numerical implementation

The equations of one–dimensional model (9)—(11) were integrated numerically by the Runge–Kutta–Merson method of 5th order with variable spacial step, which was chosen to maintain the required accuracy. For example, a fixed relative error of $5 \cdot 10^{-6}$ resulted in around 800 steps on the interval $(-L_r, L_p + L_r)$ for $L_p = 2000$, $L_r = 100$. The step size at the interfacial regions was much smaller than at the rest of the interval in order to resolve large potential, concentration, and pressure gradients there.

The governing equations of two–dimensional model (Section 2.3) were solved numerically with a help of ANSYS Fluent 14.5 (Academic version). Note that the Nernst–Planck and Poisson equations cannot be realized by means of standard ANSYS Fluent capabilities. They were implemented with the help of user–defined scalar (UDS) transport equations, which were realized through user–defined functions (UDF) library. This approach allowed setting the convection, diffusion, and migration transport terms in the Nernst–Planck equations as well as the source term in the Poisson equation. The coupling with Navier–Stokes equations was realized by introducing the corresponding source term.

Let us briefly describe the main features of numerical schemes used. The stationary problem was solved iteratively by two methods in finite volume formulation [32]. The first one is the Coupled scheme [33], which solves the pressure–based momentum and continuity equations together. The second is the SIMPLEC scheme [34], where the momentum equation is segregated from continuity equation, from which the Poisson equation for pressure is derived and solved to obtain the velocity correction. The Coupled scheme provides a robust and efficient implementation for complex flows with superior performance compared to the segregated solution scheme SIMPLEC. Approximation of convective terms in the transport equations was

carried out by the second order upwind scheme. For diffusion fluxes and source terms, the second–order approximation was employed. The linearized algebraic equations were solved by the algebraic multi–grid (AMG) iterative method for accelerated convergence. The details of numerical algorithms can be found in the ANSYS Fluent 14.5 documentation.

The characteristics of computational mesh were chosen in such a way as to ensure that further refinement did not influence the solution quality. For the typical case of $R_p = 2$ nm, $L_p = 2000$ nm, $R_r = 25$ nm, $L_r = 100$ nm, the number of nodes in radial and axial directions was 20 and 3000 for the nanopore, and 70 and 120 for each reservoir, respectively. The mesh had clustering in the axial direction near the nanopore entrance and exit as well as in the radial direction in the reservoirs. In the nanopore, the mesh was radially uniform. For other dimensions of the nanopore, the number of nodes was changed accordingly.

We have performed a comparison of convergence between formulations in Primitive variables (17)—(21) and Slotboom variables (24)—(28) as well as between Coupled and SIMPLEC methods. Figure 3 shows the dependence of residuals $\mathcal{R}$ for continuity equation (18) or (25) and negative ion transport equation (20) or (27) on the number of iterations n. One can see that the use of Slotboom variables allows to decrease the required number of iterations by 2–3 times in comparison with the use of Primitive variables. The Coupled method allows to decrease this number further by 5 times. It should be noted that the calculations were performed with the serial processing option (i.e. on a single core). It was found that the use of parallel computations significantly increases the number of iterations required for convergence.

In the calculations, it was ensured that the total fluxes of positive and negative ions obtained by summing up convection, diffusion, and migration fluxes are constant and equal at each cross–section including the interfacial regions. Additional validation was performed by comparing the results of two–dimensional model with those based on one–dimensional approach. A good agreement was found for small pore radius and low applied surface potential / charge density, where the homogeneous approximation is valid (see Section 4).

4 Results and discussion

4.1 The distributions of potential, pressure, ion concentrations and fluxes

In this section, we perform a detailed study of flow and ion transport in the nanopore and two reservoirs on the basis of one– and two–dimensional models. The dimensions of the nanopore are fixed at $R_p = 2$ nm, $L_p = 1000$ nm, the inlet ion concentration is $C^L = 10$ mol/m^3, and the volume flux is $J_V = 100$ μm/s.

The parameters of the considered cases are summarized in Table 2. In this paper, we consider nanopores with negative surface potential / charge density. Since the ratio of K^+ and Cl^- diffusion coefficients is close to unity, the solution for positive values of these parameters can be obtained by applying the change of variables (23). First, the two–dimensional model is solved for constant surface potential φ_s. Then the equivalent surface charge density σ_s is determined from the boundary condition

$$\varepsilon\varepsilon_0 \frac{\partial \Phi}{\partial r} = \sigma_s \tag{29}$$

averaged over the pore surface (here Φ is the dimensional potential). It allows one to determine the volume charge density X from (4). The potential φ is calculated by averaging the dimensional potential over the pore volume. These parameters are used in the corresponding one–dimensional models, see Sections 2.1 and 2.2.

The chosen dimensional parameters correspond to the following values of dimensionless parameters defined by (22): $\mathrm{Re} = 1.123 \cdot 10^{-5}$, $\mathrm{Pe} = 5.110 \cdot 10^{-5}$, $\Lambda = 2.486 \cdot 10^{9}$, $D = 1.038$,

Table 2: The parameters of considered cases of study: surface potential φ_s, volume–averaged potential φ, surface charge density σ_s, volume charge density X for $R_p = 2$ nm, $L_p = 1000$ nm, $C^L = 10$ mol/m^3, $J_V = 100$ μm/s.

Case	φ_s	φ	σ_s	X
	V	V	10^{-2} C/m^2	mol/m^3
1	-0.02	-0.0189	-0.159	-17
2	-0.04	-0.0372	-0.399	-41
3	-0.06	-0.0545	-0.818	-85
4	-0.08	-0.0702	-1.543	-160
5	-0.10	-0.0840	-2.726	-283
6	-0.12	-0.0958	-4.567	-473
7	-0.14	-0.1057	-7.333	-760

$\lambda = 3.042$, $J'_V = 6.4 \cdot 10^{-3}$. The dimensionless surface potential and charge density vary in the following ranges: $\varphi'_s = -0.778$ ... -5.449, $\sigma'_s = -0.089$ ... -4.107. For comparing the results obtained from one– and two–dimensional models, we introduce the cross–sectionally averaged variables:

$$\overline{\Phi} = \frac{1}{\pi R_p^2} \int_0^{2\pi} \int_0^{R_p} \Phi \, r dr d\varphi, \qquad \overline{C}_\pm = \frac{1}{\pi R_p^2} \int_0^{2\pi} \int_0^{R_p} C_\pm \, r dr d\varphi,$$

$$\overline{P} = \frac{1}{\pi R_p^2} \int_0^{2\pi} \int_0^{R_p} P \, r dr d\varphi.$$

where Φ, $C_\pm$, P are the dimensional potential, ion concentrations, and pressure, respectively. For one–dimensional model, the averaged quantities coincide with the non–averaged ones since the latter depend on z coordinate only. In addition, the convection fluxes $J_\pm^U$, diffusion fluxes $J_\pm^D$, migration fluxes $J_\pm^M$, and total fluxes $J_\pm$ of ions in axial direction are defined by

$$J_\pm^C = \int_0^{2\pi} \int_0^{R_p} C_\pm V \, r dr d\varphi, \qquad J_\pm^D = \int_0^{2\pi} \int_0^{R_p} \left(-D_\pm \frac{\partial C_\pm}{\partial z} \right) r dr d\varphi,$$

$$J_\pm^M = \int_0^{2\pi} \int_0^{R_p} \left(\mp \frac{D_\pm F}{RT} C_\pm \frac{\partial \Phi}{\partial z} \right) r dr d\varphi, \qquad J_\pm = J_\pm^C + J_\pm^D + J_\pm^M.$$

The corresponding fluxes for one–dimensional model are calculated from (1) by multiplying it to the nanopore cross–sectional area πR_p^2.

Figure 4 shows the profiles of potential, pressure, ion concentrations, and axial velocity in the central cross–section of the nanopore at $z = L_p/2$. The results for constant surface potential / charge density virtually coincide in this cross–section. Counter–ion enrichment and co–ion depletion are observed in the nanopore. For small values of φ_s or σ_s, the profiles of Φ, P, C_+ show weak dependence on the radial coordinate r. When these values are increased, pronounced radial variations are observed. The concentration of counter–ions C_+ increases, while the concentration of co–ions C_- decreases towards the pore wall. The pressure rise near

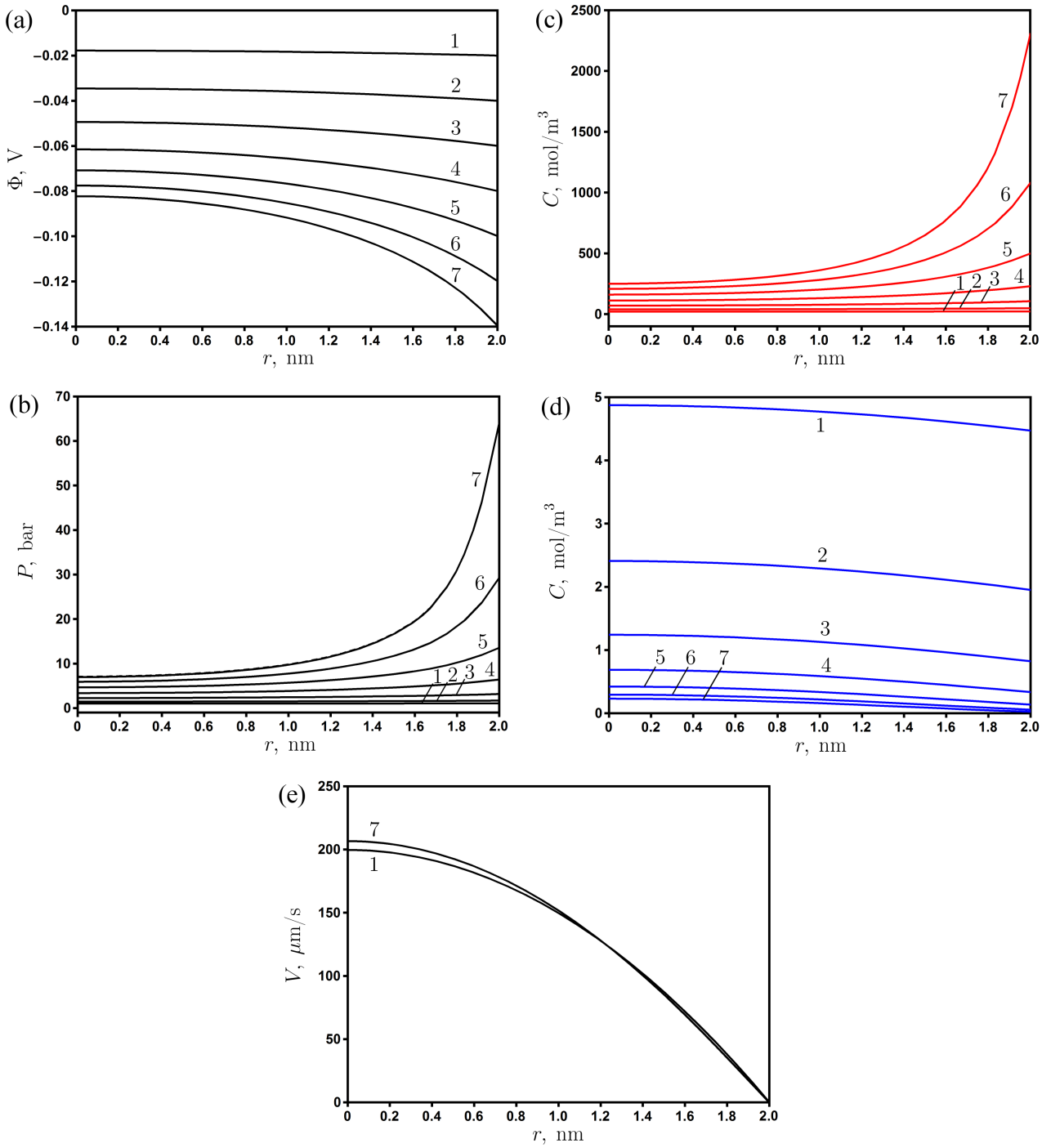

Figure 4: The distributions of potential (a), pressure (b), concentrations of positive (c) and negative (d) ions, and axial velocity (e) in the cross–section obtained from two–dimensional model. The curves correspond to Cases 1–7 in Table 2.

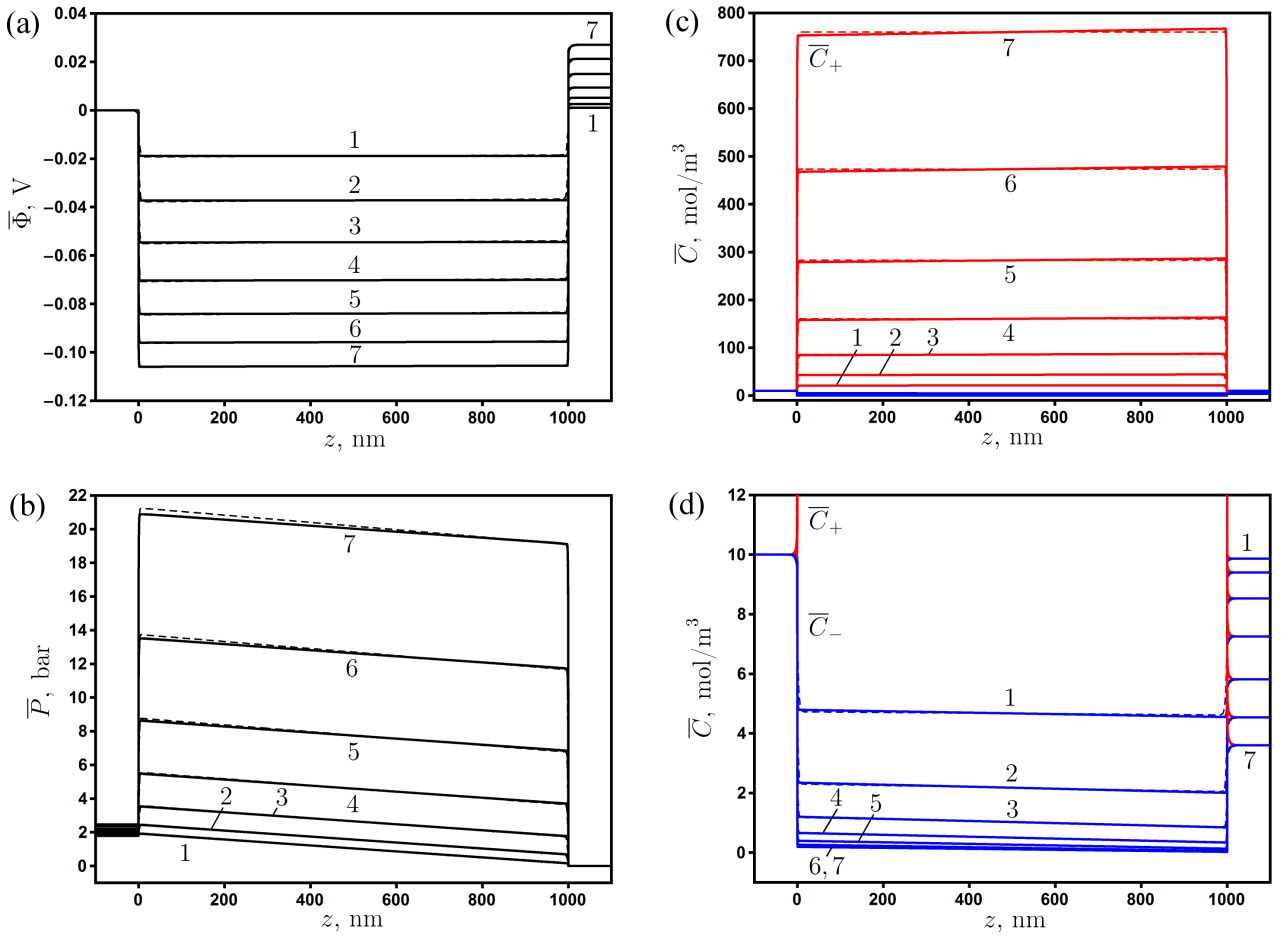

Figure 5: The distributions of averaged potential (a), pressure (b), and ion concentrations (c,d) for the case of constant surface potential (solid curves) and constant surface charge density (dashed curves) obtained from two–dimensional model. The curves correspond to Cases 1–7 in Table 2.

the wall compensates the electric force (the last term in equation (17)), which is directed towards the wall. For large potentials, the axial velocity profile shows some deviation from the purely parabolic one. The reasons for that will be discussed below after analyzing the axial profiles of all quantities.

The distributions of averaged potential, pressure, and ion concentrations obtained from the numerical solution of two–dimensional model for Cases 1–7 in Table 2 are shown in Fig. 5. One can see that the increase of surface potential φ_s or surface charge density σ_s by absolute value leads to the larger potential and osmotic pressure jumps at the entrance/exit of the nanopore. The concentration of counter–ions (K^+) increases, while that of co–ions (Cl^-) decreases inside the nanopore. The electrolyte concentration at the right reservoir becomes smaller, so the rejection of salt is enhanced. One can also observe the rise of membrane potential $\Delta\overline{\Phi} = \overline{\Phi}(L_p + L_r)$ when φ_s or σ_s are increased. The pressure gradient inside the nanopore is mainly determined by the specified volume flux J_V. The osmotic pressure jumps (see also (12), (13)) balance the electric force, which develops in the interfacial regions, where non–zero net charge is subjected to a large electric field. The total pressure drop $\Delta\overline{P} = \overline{P}(-L_r)$ increases with increasing φ_s or σ_s. The change of pressure drop due to the presence of electric force is known as electroviscous effect. Our findings are in line with previous results for low aspect ratio pores [27, 28].

Some differences between the cases of constant surface potential and constant surface

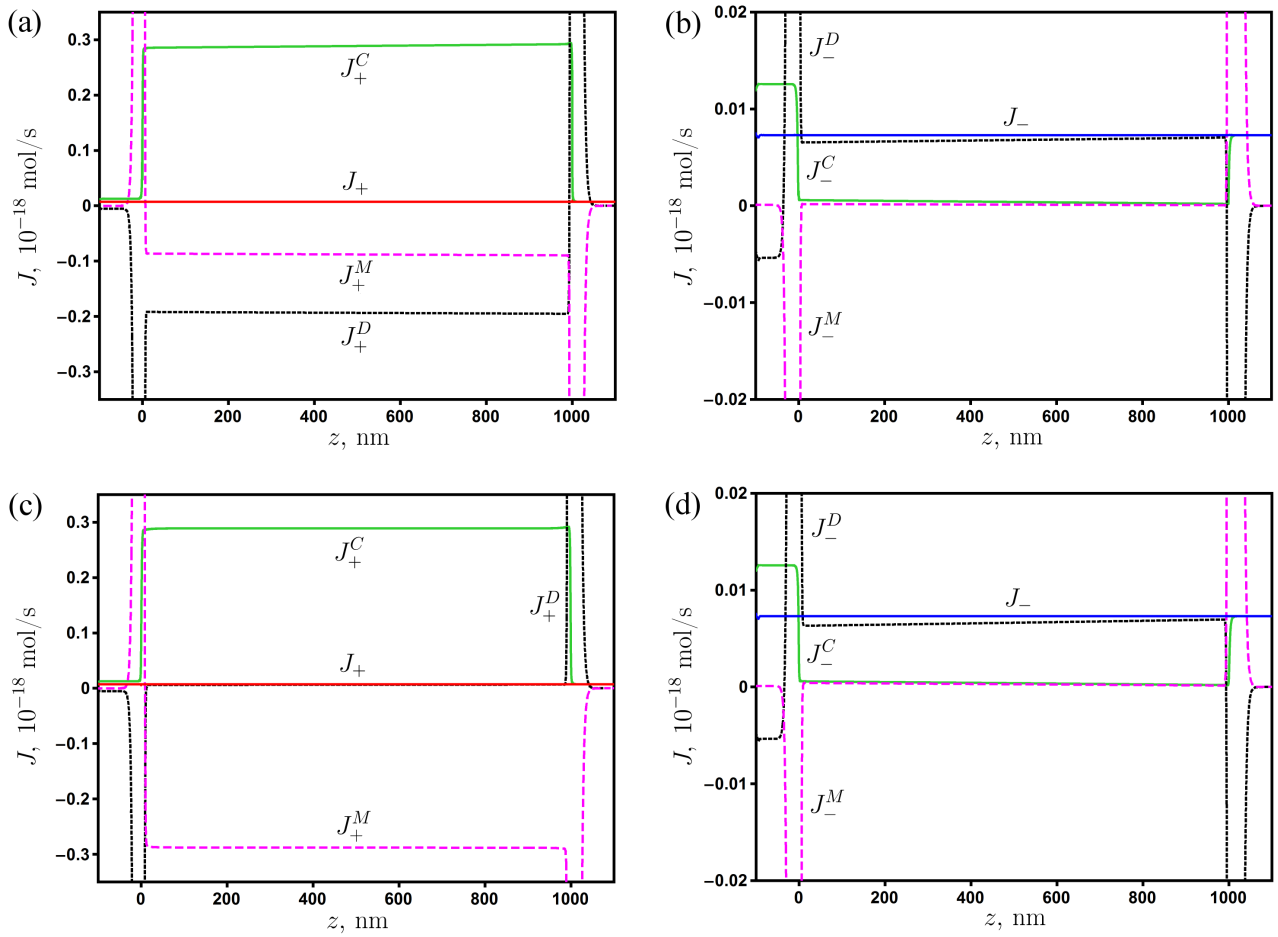

Figure 6: The distributions of ion fluxes for the case of constant surface potential (a,b) and constant surface charge density (c,d) obtained from two–dimensional model. The curves correspond to Case 5 in Table 2.

charge density can be observed from Fig. 5. In the latter case, the ion concentrations are almost constant inside the nanopore, while in the former case, notable ion concentration gradients develop there. They are directed from the nanopore entrance to the exit for counter–ions and oppositely for co–ions. The potential gradient inside the nanopore is slightly larger for $\sigma_s = \text{const}$ than for $\varphi_s = \text{const}$. The potential difference between the two ends of a charged nanopore arising due to pressure–driven flow is known as streaming potential. The increased streaming potential results in the larger electric force directed to the nanopore entrance (see the last term in equation (17)). At fixed volume flow rate J_V, the pressure gradient inside the nanopore for $\sigma_s = \text{const}$ becomes larger than that for $\varphi_s = \text{const}$ to compensate the increase of electric force. Note that in the former case, the osmotic pressure jump at the entrance (exit) is larger (smaller) than that in the latter case. These effects lead to the difference between pressure profiles for constant surface potential/charge density in Fig. 5 (b). However, the total pressure drops $\Delta\overline{P} = \overline{P}(-L_r)$ for these two cases virtually coincide.

The impact of axial electric force on the velocity profile is demonstrated in Fig. 4 (e). This force acts in the direction of nanopore entrance, and its magnitude is stronger near the nanopore walls. In this region, the flow is slightly slowed down with increasing the applied potential/charge density, while near the centerline it is enhanced to provide the same averaged volume flux J_V.

The mechanisms of ion transport the nanopore and reservoirs can be understood from the distribution of ion fluxes, which is shown in Figure 6 for Case 5 in Table 2. The total fluxes

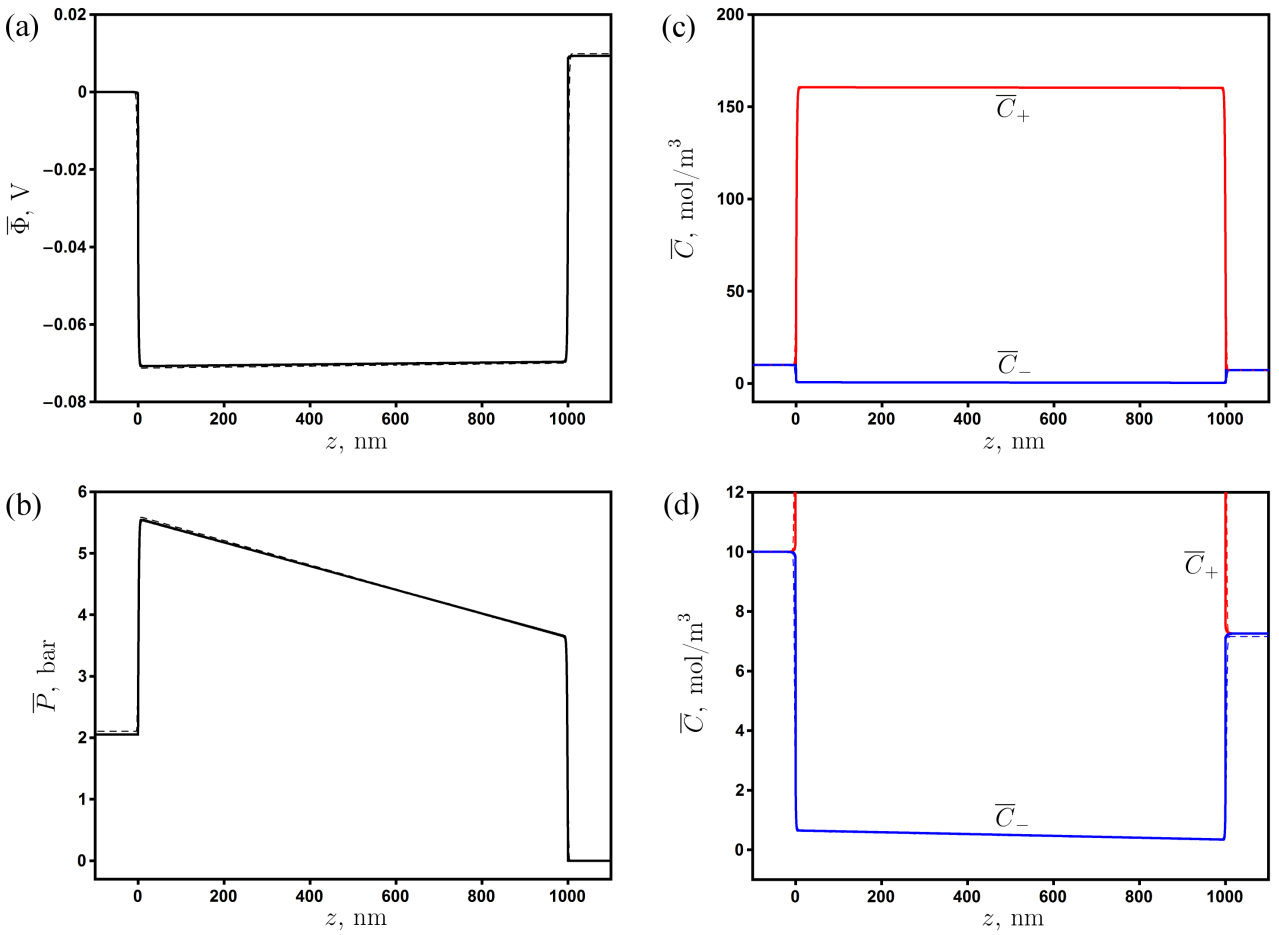

Figure 7: Comparison between the distributions of averaged potential (a), pressure (b), and ion concentrations (c,d) for two–dimensional (solid curves) and one–dimensional (dashed curves) models when the surface charge density is constant, Case 4 in Table 2.

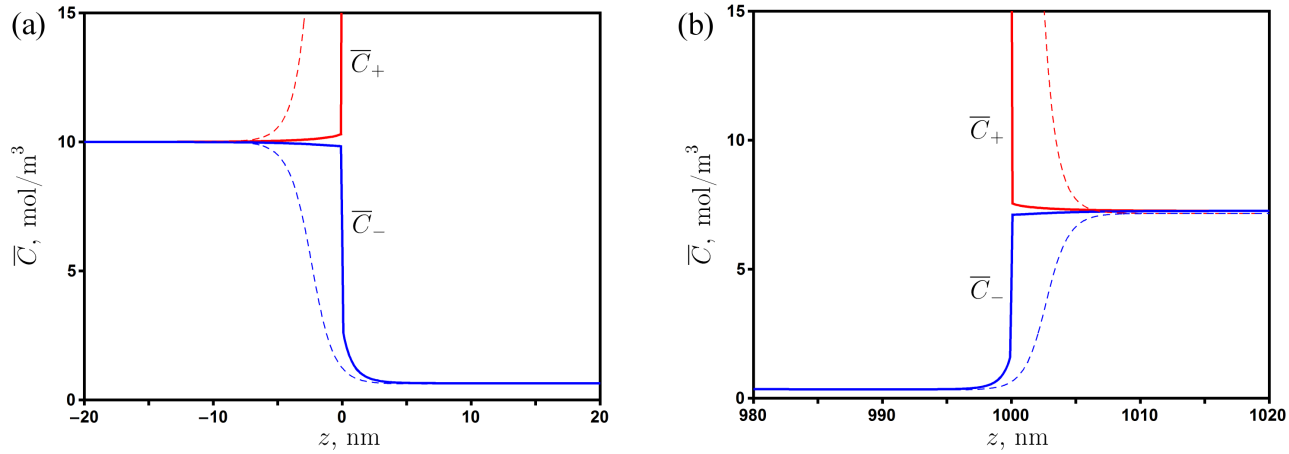

Figure 8: Comparison between the distributions of ion concentrations near the nanopore entrance (a) and exit (b) for two–dimensional (solid curves) and one–dimensional (dashed curves) models when the surface charge density is constant, Case 4 in Table 2.

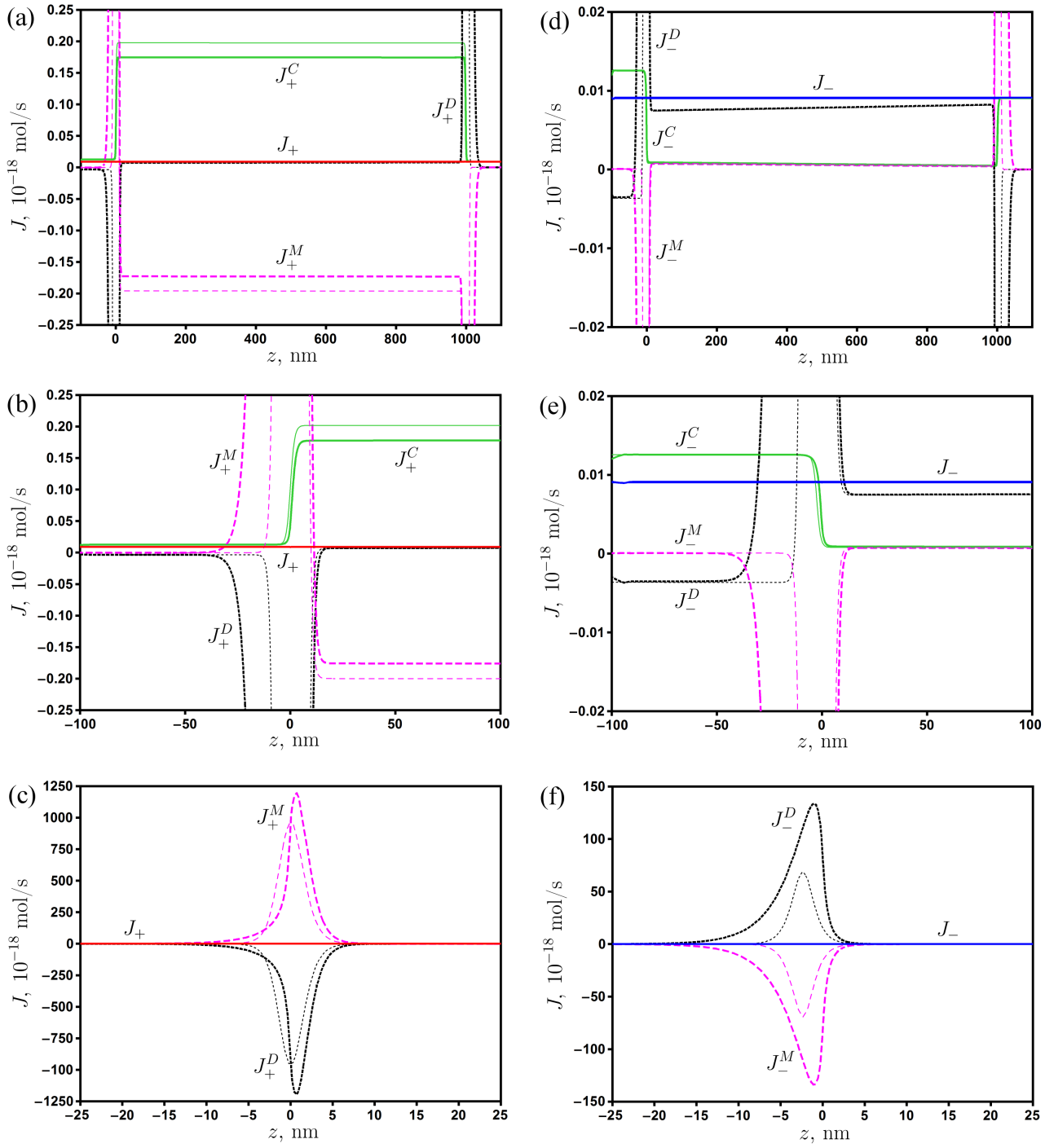

Figure 9: Comparison between the distributions of positive (a,b,c) and negative (d,e,f) ion fluxes for two–dimensional (thick curves) and one–dimensional (thin curves) models when the surface charge density is constant, Case 4 in Table 2.

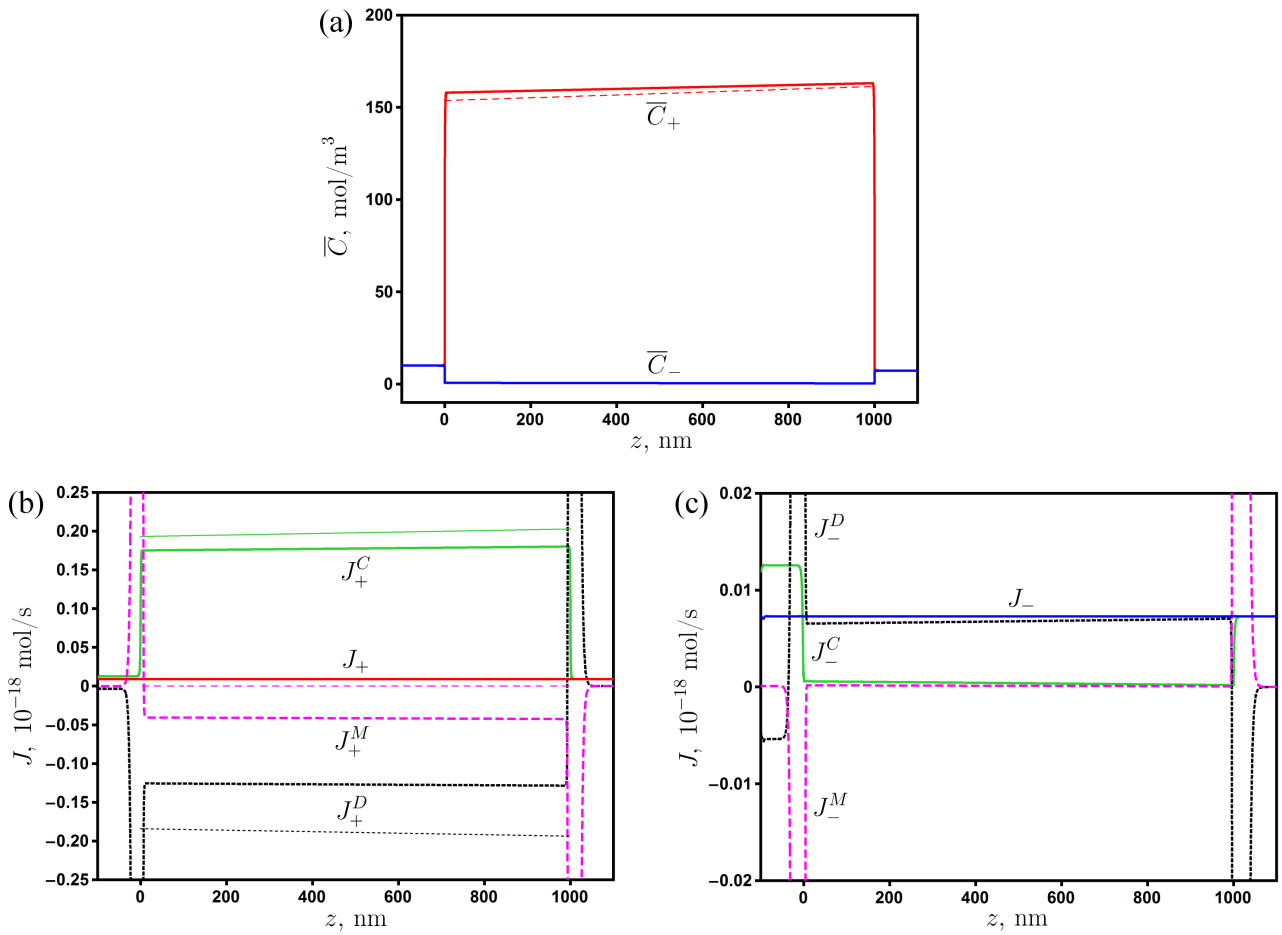

Figure 10: Comparison between the distributions of positive (a) and negative (b) ion fluxes for two–dimensional (thick curves) and one–dimensional (thin curves) models when the surface potential is constant, Case 4 in Table 2.

of ions at any cross–section are equal to the convective salt flux at the outlet of the right reservoir, i.e. $J_\pm = J_\pm^C = C^R J_V \pi R_p^2$, where $C^R = C_\pm(L_p + L_r)$. At the outlet, there are no potential and concentration gradients, so the diffusion $J_\pm^D$ and migration $J_\pm^M$ fluxes are absent. Inside the nanopore, the co–ions are mainly transported by diffusion with a small contribution from convection and migration, which is more pronounced near the nanopore entrance, see Fig. 6 (b,d). The large convective flux of counter–ions is almost completely balanced by the opposite diffusion and migration fluxes for the case of constant potential (Fig. 6 (a)) and by the opposite migration flux only for the case of constant surface charge density (Fig. 6 (b)). In the left reservoir, the ions transported by the inlet convective fluxes $J_\pm^C = C^L J_V$ are partially rejected by the opposite diffusion fluxes $J_\pm^D$. It means that the salt concentration gradient directed to the nanopore entrance is formed in the left reservoir. However, this gradient is rather small and cannot be seen in Fig. 5 (d). In the interfacial regions near nanopore entrance and exit, large migration and diffusion fluxes of ions develop and almost completely balance each other, see also Fig. 9 (c,f) below. It should be noted that large unequal migration and diffusion fluxes at the entrance / exit of a charged membrane pore were reported in [24]. In that work, the pore connected two reservoirs with equal or different concentrations in the absence of pressure–driven flow.

Comparison of results obtained from one– and two–dimensional models is presented in Fig. 7 for the constant surface charge density (Case 4 in Table 2). It can be seen that the

agreement is very good. One–dimensional model predicts slightly larger values of membrane potential and required pressure drop, and slightly smaller salt concentration at the outlet. Note that this model does not take into account the radial variations of the above quantities. Figure 8 shows a close–up view of ion concentrations near the pore entrance and exit. The difference between curves obtained from one– and two–dimensional models is observed in a short region of around 10 nm near $z = 0$ and $z = L_p$, while outside this region the curves virtually coincide. The difference is caused by the geometry of reservoirs and the value of constant k in formula (15).

The comparison between fluxes determined from one- and two–dimensional models is shown in Fig. 9 for the constant surface charge density (Case 4 in Table 2). One can see that the former model provides not only qualitative, but also quantitative agreement with the latter one. The differences are most pronounced in the interfacial regions. In particular, sharp fronts of diffusion and migration fluxes in the left reservoir are shifted closer to the nanopore entrance in one–dimensional model in comparison with two–dimensional one. Figures 9 (c) and (f) show that these fluxes are 10^4—10^5 times higher than the total fluxes of ions in the interfacial regions. Finally, it should be noted that the agreement between one– and two–dimensional models becomes better (worse) with decreasing (increasing) the surface charge density.

When the constant surface potential is specified, the agreement between the two considered models is also good for low potentials and becomes worse when the potential is increased. Note that in this case the comparison can be made only inside the nanopore, see Section 2.2. Figure 10 shows the ion concentrations and fluxes for Case 4 in Table 2. It can be seen that the volume charge density $X = C_- - C_+$ obtained from one–dimensional model with constant volume–averaged potential φ is slightly lower than that found from two–dimensional model. There is a complete agreement for total fluxes as well as for three contributions to the total flux of co–ions. For counter–ions, the two–dimensional model predicts non–zero migration flux, while this flux is absent in one–dimensional model since the potential is assumed to be constant and homogeneous in radial direction. The diffusion fluxes of counter–ions in the two models differ accordingly in order to compensate the convective flux. It follows that the one–dimensional model suggested in Section 2.2 does not fully describe the mechanisms of ion transport in the nanopore.

4.2 Rejection, pressure drop, and membrane potential

This section is focused on studying the dependence of rejection, required pressure drop, and membrane potential on the applied surface potential / charge density, volume flux, electrolyte concentration, and nanopore radius. The length of the nanopore is fixed at $L_p = 2000$ nm. For two–dimensional model, the rejection is calculated by formula (16) with $C^L = C_{\pm}(-L_r)$ and $C^R = C_{\pm}(L_p+L_r)$. The pressure drop and membrane potential are calculated as $\Delta\overline{P} = \overline{P}(-L_r)$ and $\Delta\overline{\Phi} = \overline{\Phi}(L_p + L_r)$, respectively. For one–dimensional model, $\Delta\overline{P} = \Delta P$ and $\Delta\overline{\Phi} = \Delta\Phi$.

First, the influence of variable surface potential / charge density on the nanopore selectivity is investigated for $R_p = 2$ nm, $C^L = 10$ mol/m^3, $J_V = 100$ μm/s. The considered cases of study are summarized in Table 3. The same values of φ_s as in Table 2 are taken here, while the calculated values of φ, σ_s, X are slightly different from those in Table 2 since the nanopore length is two times larger. The results of calculations are presented in Fig. 11. The horizontal axis corresponds to the values of surface potential φ_s or equivalent values of φ, σ_s, X from Table 2. One can see that the increase of surface potential / charge density by absolute value results in the increase of rejection, pressured drop, and membrane potential. The value of pressure drop in the limiting case $\varphi_s = 0$ corresponds to the hydrodynamic pressure drop of Poiseuille flow, see the second term in the right–hand side of (14).

For low values of φ_s or σ_s, the radial variations of potential, ions concentrations, and

Table 3: The parameters of considered cases of study: surface potential φ_s, volume–averaged potential φ, surface charge density σ_s, volume charge density X for $R_p = 2$ nm, $L_p = 2000$ nm, $C^L = 10$ mol/m^3, $J_V = 100$ μm/s.

Case	φ_s V	φ V	σ_s 10^{-2} C/m^2	X mol/m^3
1	−0.02	−0.0189	−0.163	−17
2	−0.04	−0.0372	−0.408	−42
3	−0.06	−0.0544	−0.835	−87
4	−0.08	−0.0700	−1.569	−163
5	−0.10	−0.0838	−2.765	−287
6	−0.12	−0.0956	−4.621	−479
7	−0.14	−0.1055	−7.403	−767

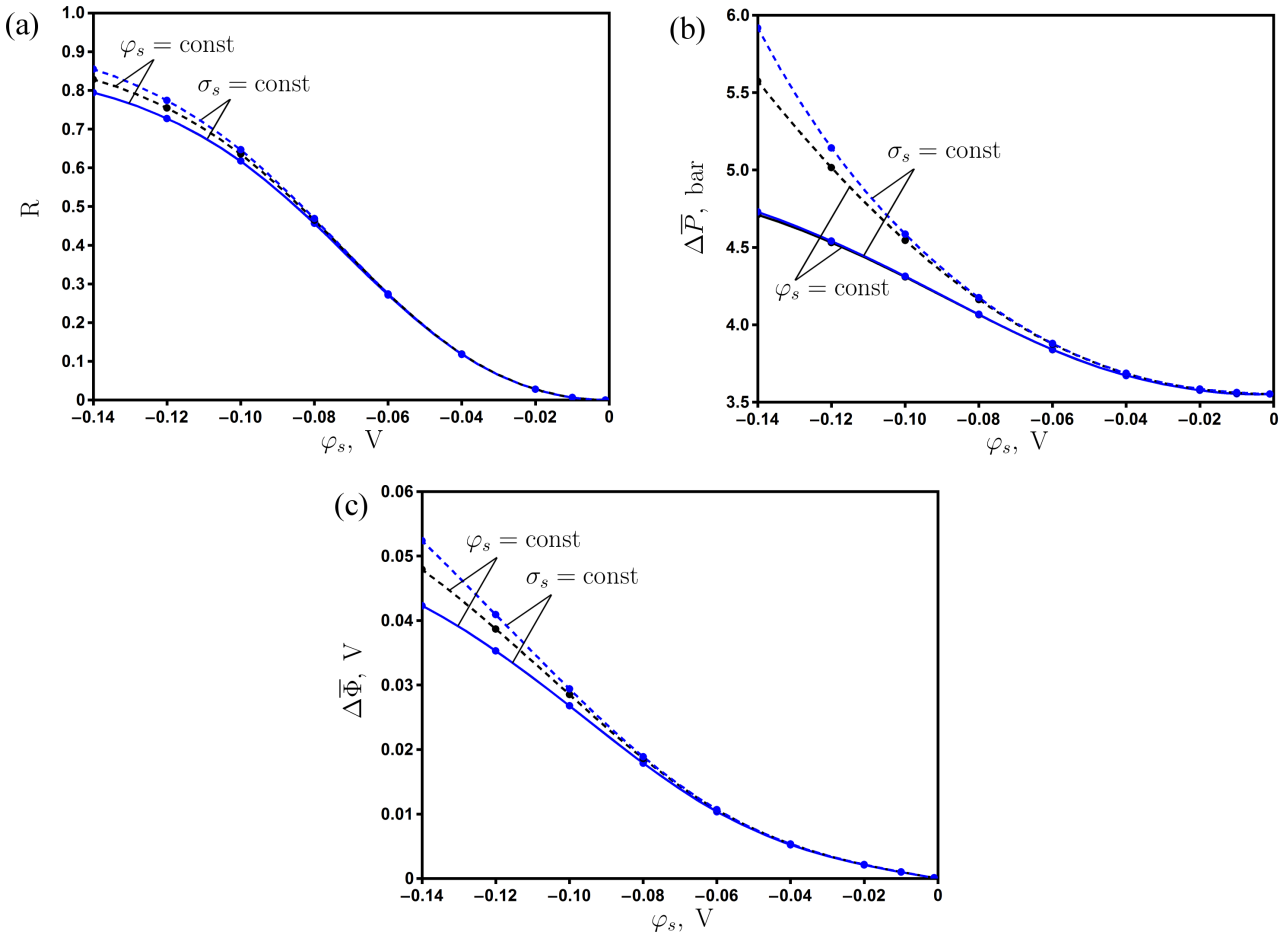

Figure 11: The dependence of rejection (a), pressure drop (b), and membrane potential (c) on the surface potential / equivalent surface charge density for one–dimensional model (dashed curves) and two–dimensional model (solid curves). The calculated cases are shown by dots, see Table 3.

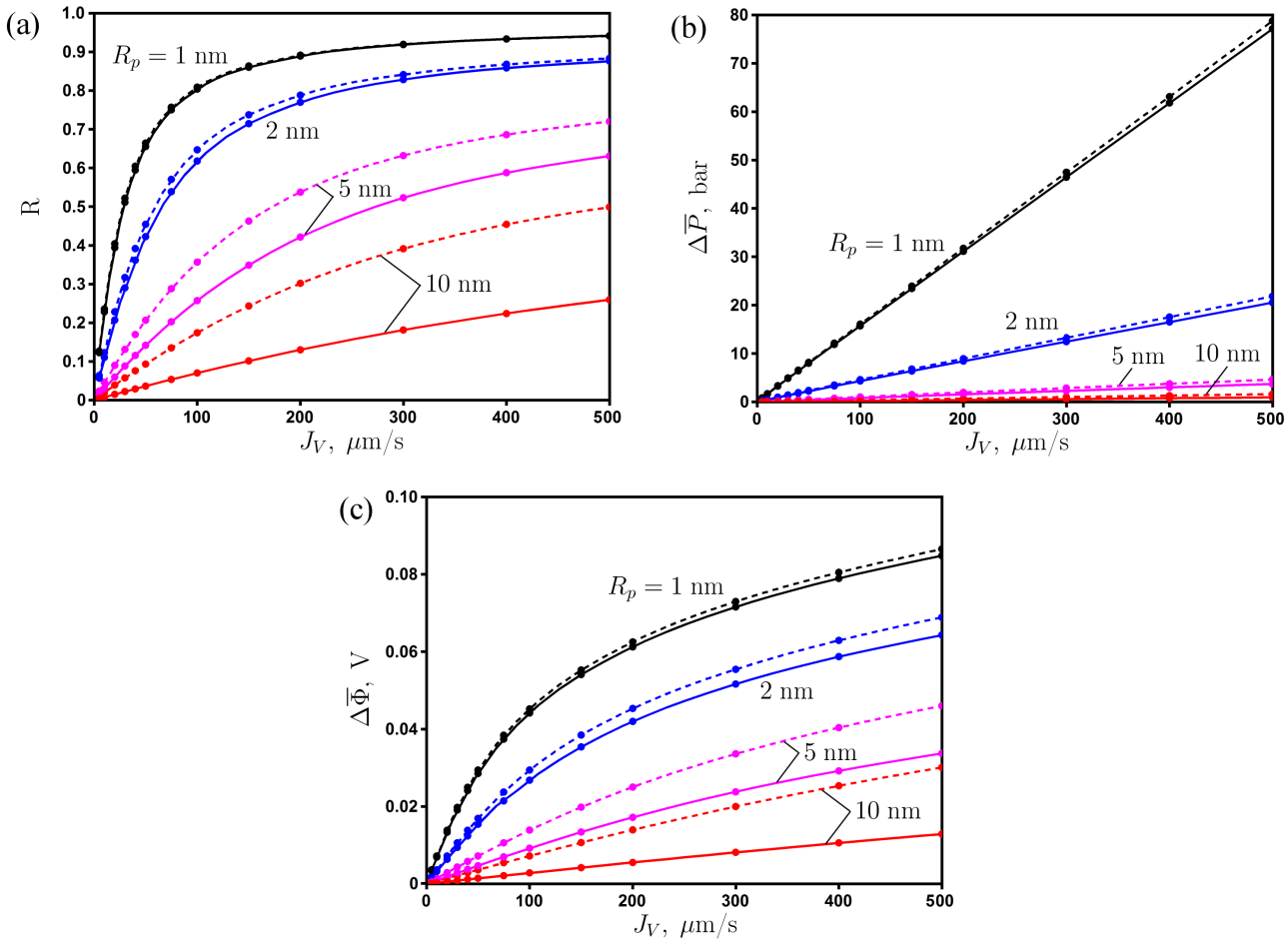

Figure 12: The dependence of rejection (a), pressure drop (b), and membrane potential (c) on the volume flux J_V for different nanopore radii R_p. One–dimensional model (dashed curves) and two–dimensional model (solid curves) for $\sigma_s = -2.765 \cdot 10^{-2}$ C/m^2, $C^L = 10$ mol/m^3.

pressure are rather small (see Fig. 4), so the agreement between one– and two–dimensional models is almost complete. With increasing the above parameters, the difference between the two models becomes evident with one–dimensional model providing overestimated values of the considered characteristics. The latter model also provides larger values of these characteristics for $\sigma_s = \text{const}$ in comparison with $\varphi_s = \text{const}$. Note that in one–dimensional models, the volume charge density X or potential φ should be specified. The equivalent value of X is obtained from two–dimensional results with the help of (4) and (29), while the equivalent potential φ is found by averaging the two–dimensional potential over the pore volume. It turns out that the average volume charge density determined from the model with constant potential on the basis of first equation in (3) is lower than the value taken in the model of constant surface charge. For example, the solution for $\varphi = -0.1055$ V provides $X = -640$ mol/m^3, while the corresponding value of X in Table 3 is -767 mol/m^3 (see Case 7). It explains the differences between results of one–dimensional models in Fig. 11. Note that in the model of constant potential, the contribution of electric force to the pressure gradient is absent inside the nanopore, see (11) and (14). Thus, the pressure drop in this case should be lower in comparison with that for constant surface charge density. Finally, the two–dimensional models for constant surface potential / charge density provide nearly the same results.

Figure 12 shows the dependence of rejection, pressure drop, and membrane potential on the volume flux J_V for different nanopore radii R_p with $\sigma_s = -2.765 \cdot 10^{-2}$ C/m^2 and $C^L = 10$

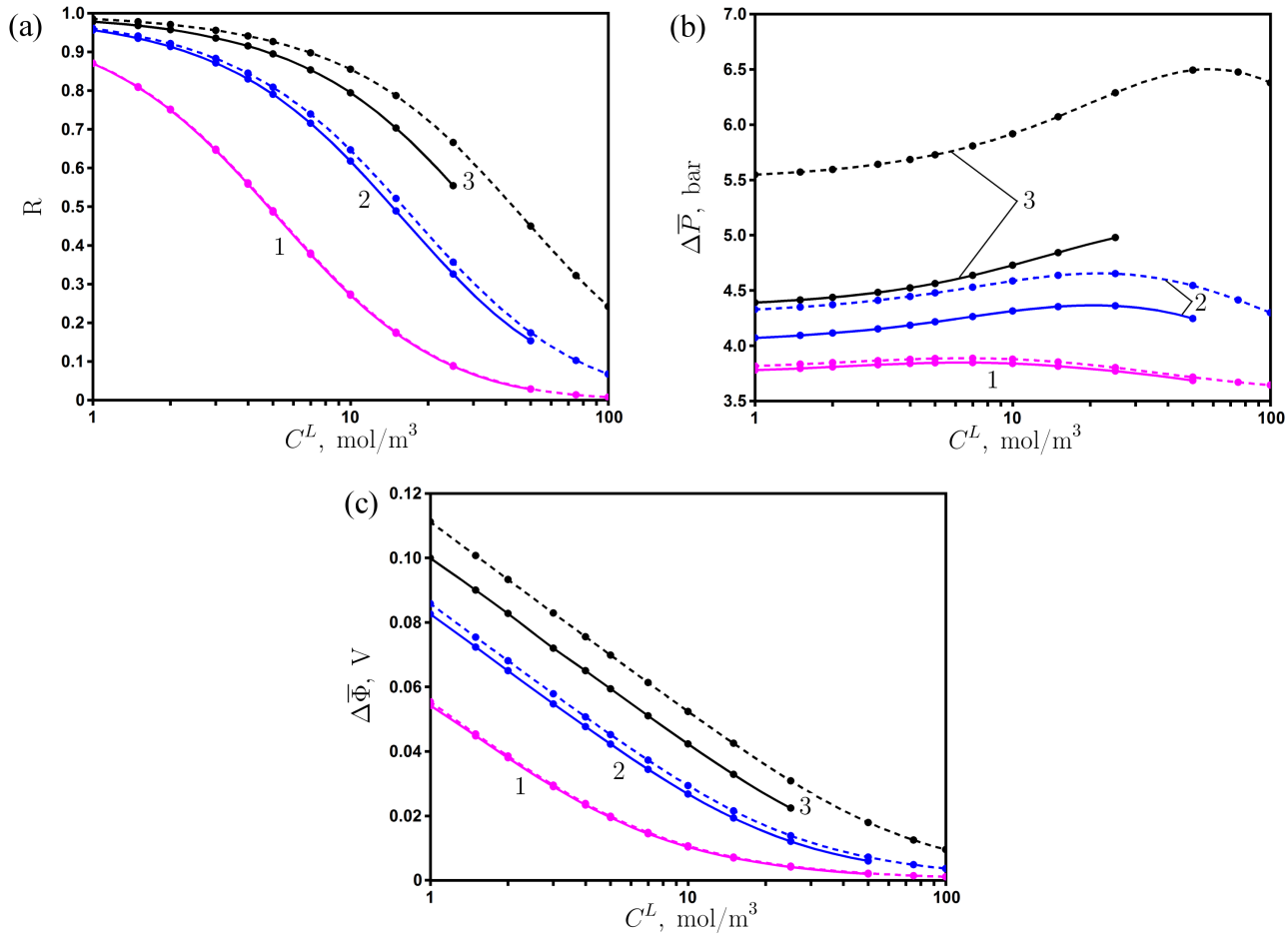

Figure 13: The dependence of rejection (a), pressure drop (b), and membrane potential (c) on the inlet concentration C^L for different surface charge density $\sigma_s = -0.835 \cdot 10^{-2}$ C/m^2 (1), $-2.765 \cdot 10^{-2}$ C/m^2 (2), $-7.403 \cdot 10^{-2}$ C/m^2 (3). One–dimensional model (dashed curves) and two–dimensional model (solid curves) for $R_p = 2$ nm.

mol/m^3. For this value of inlet concentration, the Debye length is 3.042 nm. When the nanopore radius is smaller than the Debye length, electric double layers from the opposite walls overlap, so the radial variations of potential, ion concentrations, and pressure are not large. In this case, the results from one–dimensional model agree well with those from two–dimensional one. However, the latter model provides overestimated values of the considered characteristics. The overestimation of rejection and membrane potential becomes significant with increasing the nanopore radius. The differences in pressure drop are rather small since it is mainly determined by the the specified volume flux. The increase of J_V results in larger values of pressure drop, membrane potential, and rejection. The latter approaches some limiting value for high volume flux and small nanopore radius. The obtained results on rejection show similar trends in comparison with the results reported earlier in [21], where the TMS and Space–charge models were compared.

The impact of inlet concentration C^L on rejection, pressure drop, and membrane potential for the nanopore of radius $R_p = 2$ nm and volume flux $J_V = 100$ μm/s is presented in Fig. 13 for different surface charge densities σ_s. Larger values of σ_s correspond to higher rejection, membrane potential, and pressure drop. The difference between results from one– and two–dimensional models becomes more pronounced. The former model provides overestimated values of the considered quantities. The increase of inlet concentration C^L leads to the decrease

of Debye length (see formulas (22)). When the Debye length is smaller than the channel radius, the electric double layers from the opposite walls do not overlap, and nanopore selectivity reduces. It results in the lower rejection and membrane potential.

Figure 13 (b) shows that the pressure drop reaches the maximum value at some particular inlet concentration. Since the volume flux J_V is constant, the hydrodynamic contribution to the pressure drop is fixed. The variation of $\Delta\overline{P}$ with C^L can be explained by considering the osmotic pressure jumps at the nanopore entrance and exit, which are given by (12) and (13). When the surface charge density σ_s or equivalent volume charge density X is negative and large, we have $C_- \sim 0$ inside the nanopore. Then it follows from (3) that $C_+ \sim -X$, so the total contribution of osmotic pressure jumps can be represented as

$$-\Delta P^L - \Delta P^R \sim 2RT(C^L - C^R) = 2RTC^L\mathrm{R} \geqslant 0,$$

where R is the rejection defined by (16). When $C^L \to 0$, we have $\mathrm{R} \to 1$, so $2RTC^L\mathrm{R} \to 0$. From the other hand, when C^L becomes very large, the rejection $\mathrm{R} \to 0$ since $C^R \to C^L$. It follows that $2RT(C^L - C^R) \to 0$. Thus, the contribution of osmotic pressure jumps should reach maximum at some value of inlet concentration.

For large inlet concentrations, the curves of two–dimensional model in Fig. 13 are not calculated since the values of C_+ near the nanopore wall become non–physical. The maximum ion concentration can be estimated from the expression for volume fraction of ions $\nu = a^3 N_A C$, where a is the diameter of solvated ion, N_A is the Avogadro number, and C is the concentration of positive or negative ions in mol/m^3 [35]. If we put $\nu = 1$, then $C_{\max} = (a^3 N_A)^{-1}$. For K^+ ions, $a = 0.66$ nm, so $C_{max} = 5778$ mol/m^3. In particular, the value of C_+ near the pore wall in the case of $\sigma_s = -2.765 \cdot 10^{-2}$ C/m^2, $C^L = 25$ mol/m^3 is already very close to the above value of C_{max}. To prevent the non–physical rise of concentration at large potentials / charge densities, the finite ion size effects should be taken into account [35]. Note that this problem does not arise in one–dimensional model, where radial variations of all quantities are neglected.

5 Conclusion

In this paper, the pressure–driven ion transport through nanofiltration membrane pores with specified surface potential or charge density has been investigated theoretically. Two approaches are employed in the study. The first one is based on one–dimensional Nernst–Planck equation coupled with electroneutrality, zero current, and Donnan equilibrium conditions. This model is extended to account for interfacial effects by using a smooth approximation of step function for the volume charge density. A simplified model for the case of specified surface potential is also proposed. The second approach is based on two–dimensional Nernst–Planck, Poisson, and Navier–Stokes equations, which are solved in a high aspect ratio nanopore connecting two reservoirs with a larger diameter. The modification of equations on the basis of Slotboom transformation is employed to speed up the convergence rate.

The distributions of potential, pressure, ion concentrations and fluxes due to convection, diffusion, and migration in the nanopore and reservoirs are discussed and analyzed. It is found that for constant surface charge density, the convective flux of counter–ions in the nanopore is almost completely balanced by the opposite migration flux, while for the constant surface potential, the convective flux is balanced by the opposite diffusion and migration fluxes. The co–ions in the nanopore are mainly transported by diffusion. In the interfacial regions near nanopore entrance and exit, the fluxes due to migration and diffusion are several orders of magnitude higher in comparison with those inside the nanopore. These fluxes almost completely balance each other. In the inlet reservoir, the ions are transported by convection and partially rejected by diffusion in the opposite direction. We have shown that the axial potential gradient

induces electric force, which is directed to the nanopore entrance and acts on the non–zero net charge near the nanopore walls. As a result, the axial velocity is slightly decreased near the walls and increased near the center of the nanopore to keep volume flux constant.

We have found that the rejection, pressure drop, and membrane potential increase with increasing surface potential / charge density and volume flux, while they decrease with increasing the pore radius and inlet concentration. An exception from the latter rule is the pressure drop, which reaches maximum at some value of inlet concentration when other parameters are fixed. This effect is related to the contribution of osmotic pressure jumps at the nanopore entrance and exit. Detailed comparison between one– and two–dimensional models has been performed. It is found that they provide qualitative and quantitative agreement when the surface potential or charge density are sufficiently low. In this case, the interfacial effects can be correctly described by one–dimensional model by using a smooth approximation of step function for volume charge density. For large values of surface potential / charge density, one–dimensional model provides overestimated values of rejection, pressure drop, and membrane potential.

Acknowledgement

This work is supported the Russian Science Foundation, Project 15–19–10017.

References

[1] H. Strathmann. Introduction to membrane sceince. Wiley–VCH, 2011.

[2] R.W. Baker. Membrane technology and applications. John Wiley & Sons, 2004.

[3] P. Eriksson. Nanofiltration extends the range of membrane filtration. Enviroment. Progr. 7 (1988) 58–62.

[4] V.V. Volkov, B.V. Mchedlishvili, V.I. Roldugin, S.S. Ivanchev, A.B. Yaroslavtsev. Membranes and nanotechnologies. Nanotechnologies in Russia, 3 (2008) 656-687.

[5] M. Nishizawa, V.P. Menon, C.R. Martin. Metal nanotubule membranes with electrochemically switchable ion–transport selectivity. Science, 268 (1995).

[6] M.S. Kang, C.R. Martin. Investigations of potential–dependent fluxes of ionic permeates in gold nanotubule membranes prepared via the template method. Langmuir, 17 (2001) 2753–2759.

[7] G. Pourcelly, V.V. Nikonenko, N.D. Pismenskaya, A.B. Yaroslavtsev. Applications of charged membranes in separation, fluid cells, and emerging process. Chapter 20 in 'Ionic interactions in natural and synthetic macromolecules', John Wiley & Sons, 2012.

[8] X.L. Wang, Y.Y. Fang, C.H. Tu, B. Van der Bruggen. Modelling of the separation performance and electrokinetic properties of nanofiltration membranes. Int. Rev. Phys. Chem. 31 (2012) 111–130.

[9] V.V. Nikonenko, A.B. Yaroslavtsev, G. Pourcelly. Ion transfer in and through charged membranes: structure, properties, and theory. Chapter 9 in 'Ionic interactions in natural and synthetic macromolecules', John Wiley & Sons, 2012.

[10] T. Tsuru, S. Nakao, S. Kimura. Calculation of ion rejection by extended Nernst–Planck equation with charged reverse osmosis membranes for single and mixed electrolyte solutions. J. Chem. Eng. Jpn. 24 (1991) 511–517.

[11] T. Tsuru, M. Uralri, S. Nakao, S. Kimara. Reverse osmosis of single and mixed electrolytes with charged membranes. Experiment and analysis, J. Chem. Eng. Jpn., 24 (1991) 518.

[12] W.M. Deen, B. Satvat, J.M. Jamieson. Theoretical model for glomerular filtration of charged solutes. Amer. J. Physiology. 238 (1980) 126–139.

[13] W.R. Bowen, H. Mukhtar. Characterisation and prediction of separation performance of nanofiltration membranes. J. Membr. Sci. 112 (1996) 263–274.

[14] J. Schaep, C. Vandecasteele, A.W. Mohammad, W.R. Bowen. Analysis of the salt retention of nanofiltration membranes using the Donnan–Steric partitioning pore model. Sep. Sci. Tech. 35 (1999) 3009–3030.

[15] C. Labbez, P. Fievet, A. Szymczyk, A. Vidonne, A. Foissy, J. Pagetti. Analysis of the salt retention of a titania membrane using the 'DSPM' model: effect of pH, salt concentration and nature. J. Membr. Sci. 208 (2002) 315–329.

[16] S. Bhattacharjee, J.C. Chen, M. Elimelech. Coupled model of concentration polarization and pore transport in crossflow nanofiltration. AIChE J. 47 (2001) 2733–2745.

[17] A. Szymczyk, C. Labbez, P. Fievet, A. Vidonne, A. Foissy, J. Pagetti. Contribution of convection, diffusion and migration to electrolyte transport through nanofiltration membranes. Adv. Colloid Interface Sci. 103 (2003) 77–94.

[18] A. Szymczyk, H. Zhu, B. Balannec. Pressure–driven ionic transport through nanochannels with inhomogenous charge distributions. Langmuir 26 (2010) 1214–1220.

[19] A. Szymczyk, H. Zhu, B. Balannec. Ion rejection properties of nanopores with bipolar fixed charge distributions. J. Chem. Phys. 114 (2010) 10143–10150.

[20] R.J. Gross, J.F. Osterle. Membrane transport characteristics of ultrafine capillaries. J. Chem. Phys. 49 (1968) 228–234.

[21] X.L. Wang, T. Tsuru, S.I. Nakao, S. Kimura. Electrolyte transport through nanofiltration membranes by the space–charge model and the comparison with Teorell–Meyer–Sievers model. J. Membr. Sci. 103 (1995) 117–133.

[22] W.J. Shang, X.L. Wang, Y.X. Yu. Theoretical calculation on the membrane potential of charged porous membranes in 1–1, 1–2, 2–1 and 2–2 electrolyte solutions. J. Membr. Sci. 285 (2006) 362–375.

[23] G. Jacazio, R.F. Probstein, A.A. Sonin, D. Yung. Electrokinetic salt rejection in hyperfiltration through porous materials. Theory and experiment. J. Phys. Chem. 76 (1972) 4015–4023.

[24] R. Chein, H. Chen, C. Liao. Investigation of ion concentration and electric potential distributions in charged membrane/electrolyte systems. J. Membr. Sci. 342 (2009) 121–130.

[25] V. García–Morales, J. Cervera, J.A. Manzanares. Pore entrance effects on the electrical potential distribution in charged porous membranes and ion channels. J. Electroanalyt. Chem. 599 (2007) 203–208.

[26] Y. Wang, K. Pant, Z. Chen, G. Wang, W.F. Diffey, P. Ashley, S. Sundaram. Numerical analysis of electrokinetic transport in micro–nanofluidic interconnect preconcentrator in hydrodynamic flow. Microfluid Nanofluid 7 (2009) 683–696.

[27] M.R. Davidson, D.J.E. Harvie. Electroviscous effects in low Reynolds number liquid flow through a slit–like microfluidic contraction. Chem. Eng. Sci. 62 (2007) 4229–4240.

[28] R.P. Bharti, D.J.E. Harvie, M.R. Davidson. Steady flow of ionic liquid through a cylindrical microfluidic contraction–expansion pipe: Electroviscous effects and pressure drop. Chem. Eng. Sci. 63 (2008) 3593–3604.

[29] B. Lu, M.J. Holst, J.A. McCammon, Y.C. Zhou. Poisson–Nernst–Planck equations for simulating biomolecular diffusion–reaction processes I: Finite element solutions. J. Comp. Phys. 229 (2010) 6979–6994.

[30] J.F. Pietschmann, M.T. Wolfram, M. Burger, C. Trautmann, G. Nguyen, M. Pevarnik, V. Bayere, Z. Siwy. Rectification properties of conically shaped nanopores: consequences of miniaturization. PCCP 15 (2013) 16917.

[31] D. Menga, B. Zhenga, G. Lin, M.L. Sushko. Numerical solution of 3D Poisson–Nernst–Planck equations coupled with classical density functional theory for modeling ion and electron transport in a confined environment. Comm. Comput. Phys. 16 (2014) 1298–1322.

[32] T.J. Chung. Computational fluid dynamics. Cambridge University Press, 2010.

[33] R.F. Hanby, D.J. Silvester, J.W. Chew. A comparison of coupled and segregated solution techniques for incompressible swirling flow. Int. J. Numer. Methods in Fluids 22 (1996) 353–373.

[34] J.P. Vandoormaal, G.D. Raithby. Enhancements of the SIMPLE method for predicting incompressible fluid flows. Numer. Heat Transfer 7 (1984) 147–163.

[35] M.Z. Bazant, M.S. Kilic, B.D. Storey, A. Ajdari. Towards an understanding of induced–charge electrokinetics at large applied voltages in concentrated solutions. Adv. Colloid Interface Sci. 152 (2009) 48–88.